Soft Matter

PAPER

View Article Online
View Journal | View Issue

Cite this: *Soft Matter*, 2019, **15**, 8543

Hard topological *versus* soft geometrical magnetic particle transport†

Anna M. E. B. Rossi,[a] Jonas Bugase,[ab] Thomas Lachner,[a] Adrian Ernst,[a] Daniel de las Heras[c] and Thomas M. Fischer*[a]

The question of how a dissipative geometrical transport system changes towards a topological transport system is important to render a fragile transport into a robust transport. We show how a macroscopic magnetic topological transport of solid state spheres changes to a geometrical transport of ferrofluid droplets, when instead of a solid state object, soft matter is transported. The key difference when comparing solid objects with fluid droplets is the possibility to split a ferrofluid droplet into two droplets. It is shown how this fundamental difference also fundamentally changes the transport properties. Hence, experimentally and theoretically the transport on top of a periodic two-dimensional hexagonal magnetic pattern of (i) a single macroscopic steel sphere, (ii) a doublet of wax/magnetite composite spheres, and (iii) an immiscible mixture of ferrofluid droplets with a perfluorinated liquid is analyzed. The transport of all these magnetic objects is achieved by moving an external permanent magnet on a closed modulation loop around the two-dimensional magnetic pattern. The transport of one and also that of two objects per unit cell is topologically protected and characterized by discrete displacements of the particles as we continuously scan through a family of modulation loops. The direction and the type of transport are characterized by the winding numbers of the modulation loops around special objects in control space, which is the space for the possible directions of the external magnetic field. The winding numbers necessary for characterizing the topological transport increase with the number of particles per unit cell. The topological character of the transport is destroyed, when transporting a large collection of particles per unit cell, like it is in the case of a macroscopic assembly of magnetic nanoparticles in a ferrofluid droplet for which the transport is geometrical and no longer topological. To characterize the change in the transport from topological to geometrical, we perform computer simulations of the transport of an increasing number of particles per unit cell.

Received 10th July 2019,
Accepted 4th October 2019

DOI: 10.1039/c9sm01401b

rsc.li/soft-matter-journal

1 Introduction

When a system is driven adiabatically, its state changes slower than any relaxation time. The state of a classical system then follows the same path independently of the speed of driving. If driven adiabatically at different speeds, the state of a quantum system also follows the same path up to the global dynamic phase[1] of its wave function that cannot be measured. Measurable quantities are geometrical in the adiabatic limit, since they can be deduced from the path without the knowledge of a particular time table with which one drives the system along this path. For a periodically driven system, the transport of particles over a period then is proportional to the geometric quantity of the loop of the driving field.[2–4] For example, autonomous low Reynolds number swimmers propel by a distance proportional to the area of the driving control loop in shape space.[5,6] Adiabatic quantum two-band electrons propel by an amount proportional to the area enclosed by the SU(2), respectively $SO(3) \cong SU(2)/\mathbb{Z}_2$ matrices of the periodic control loop induced by the external field.[1,7]

The area of a loop is a geometric quantity that continuously changes when the driving control loop is altered. When symmetries or other conditions constraint the driving loop, the geometrical properties might become discrete global properties, called topological invariants. Then, the transport no longer changes continuously with the loop since families of loops share the same topological invariant. The transport changes discretely between two families of loops with different values of the topological invariant.[7] The transport is robust because it is

[a] *Experimentalphysik X, Physikalisches Institut, Universität Bayreuth, D-95440 Bayreuth, Germany. E-mail: Thomas.Fischer@uni-bayreuth.de*
[b] *University for Development Studies, Department of Applied Physics, Tamale, Ghana*
[c] *Theoretische Physik II, Physikalisches Institut, Universität Bayreuth, D-95440 Bayreuth, Germany*

† Electronic supplementary information (ESI) available. See DOI: 10.1039/c9sm01401b

topologically protected. For example, in a nucleus one nucleon must rotate by multiples of 2π when it propels by one lattice constant above the lattice of the crystallized nucleons that form the rest of the nucleus.[8]

Understanding how a system changes from geometrical towards topological is important. With this knowledge we can change a fragile, geometric transport into a robust topological transport. For example, in the quantum Hall effect steps between the plateaus in the conductivity can be created either by lowering the temperature or by using clean systems with fewer impurities.[9] Both methods decrease the probability of exciting unoccupied bulk Landau levels and thus make the system topological. For many quantum and classical systems,[10–15] the transition from geometric towards topological transport can be understood *via* the amount of dissipation occurring due to the scattering between states. It has, however, been shown that there exist non-Hermitian quantum and dissipative classical topological transport systems,[16–20] where it is precisely the dissipation that causes the topological character of the transport. For these systems the transition from topological towards geometrical must be different.

The purpose of this work is to show how topological transport phenomena also play a role in soft matter systems. We show experimentally and with computer simulations that a macroscopic topological magnetic particle pump,[21] which transports paramagnetic or soft magnetic particles across a magnetic lattice, is topological when transporting a small number of particles per unit cell. The transport is robust for the modulation loops of a driving homogeneous external field that share the same topological invariant. Subclasses of modulation loops appear for a loading with two or more particles per unit cell, increasing the number of discrete steps. However, for loadings with a macroscopic ensemble of magnetic nanoparticles, such as a ferrofluid droplet, the topological nature of the transport is destroyed and becomes geometrical.

2 Topogeometrical pump

The system consists of a two-dimensional hexagonal magnetic pattern made of up- and down-magnetized magnets, see Fig. 1a. The pattern creates a two-dimensional magnetic potential that acts on paramagnetic objects located above the pattern at fixed elevation. The potential is a function of the position $\mathbf{x}_{\mathcal{A}} \in \mathcal{A}$ of the paramagnetic object in action space $\mathcal{A}$, which is the plane parallel to the pattern in which the objects are located. A uniform external magnetic field is also applied to the system. Hence, the total potential depends parametrically on the direction of the superimposed external magnetic field. Paramagnetic objects, such as soft magnetic spheres and ferrofluid droplets move in action space when we adiabatically modulate the total potential by changing the direction of the uniform external field.

Our two dimensional magnetic hexagonal lattice is built from an arrangement of NbB-magnets[21] (Fig. 1a). The arrangement is such that the primitive unit cell of the lattice is a sixfold symmetric C_6 hexagon with corners centered within the smaller magnets, see Fig. 1b. Each unit cell thus contains one large magnet and two small magnets. The total magnetic field is the sum of the pattern $\mathbf{H}_p$ and the external $\mathbf{H}_{ext}$ contributions

$$\mathbf{H} = \mathbf{H}_p + \mathbf{H}_{ext}. \quad (1)$$

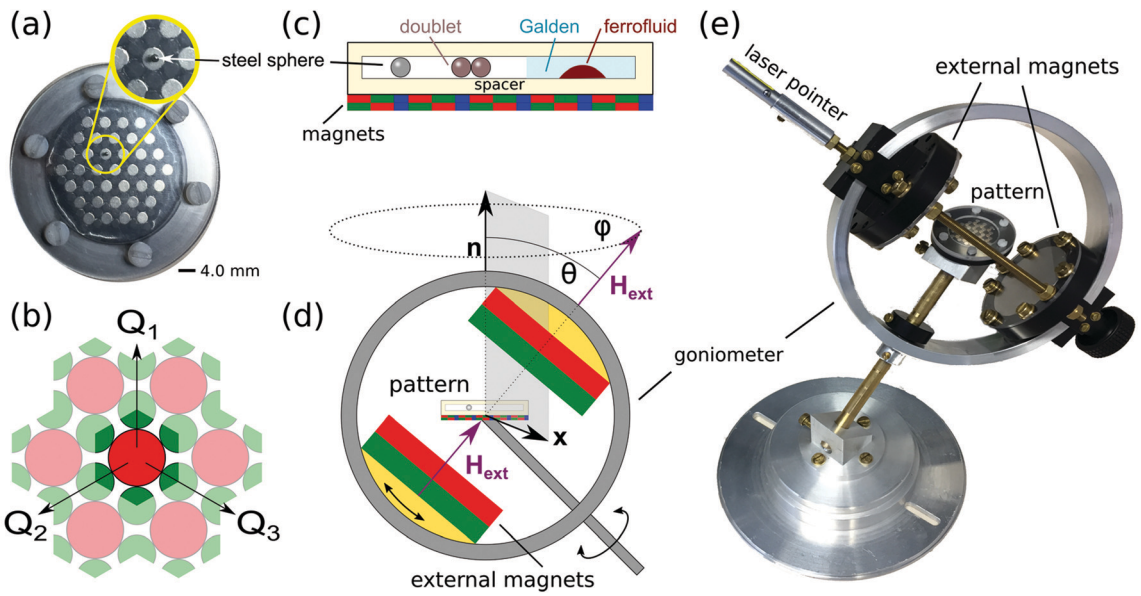

Fig. 1 Experimental setup: (a) top view of the hexagonal magnetic pattern. The inset is a close view of the transported steel sphere. (b) Scheme of the position and the orientation of the magnets. The silver areas in the sample (red areas in the scheme) are magnetized up. The black (green) areas are magnetized down. One unit cell is emphasized in full colors. The vector $\mathbf{Q}_1$ is one of the primitive reciprocal lattice vectors. (c) Side view of the pattern and the compartment holding either one steel sphere, two wax spheres, or Galden and a ferrofluid. (d) Schematic of the goniometer and the external magnets surrounding the sample. (e) A photo of the setup.

The potential energy of a paramagnetic object in the total magnetic field H is proportional to the square of the magnetic field

$$U(\mathbf{x}_{\mathcal{A}}) \propto -\mathbf{H}^2, \quad (2)$$

and it can be decomposed into a discrete Fourier series of contributions from reciprocal lattice vectors.[17,23] The Fourier series of the potential evaluated in a plane above the pattern and parallel to it is the square of the Fourier series of the magnetization of the pattern augmented by the external field. As a function of elevation, the higher Fourier coefficients are attenuated more than those with lower reciprocal vectors. At the experimental elevation (comparable to the length of the unit cell of the pattern), only the "universal" contributions to the potential from the lowest non-zero reciprocal lattice vectors remain relevant.[17,23] The purpose of the spacer (Fig. 1c) is thus to render the potential universal such that only the symmetry and not the fine details of the pattern are important.

We either place one steel sphere or two spheres consisting of a mixture of wax and magnetite on top of the spacer. Alternatively, we fill a closed compartment with a mixture of a nonmagnetic fluid (Galden) and an aqueous ferrofluid, immiscible with the Galden. The choice of particles and ferrofluids to be transported is made in a way as to suppress dipolar interactions and fingering instabilities[24,25] that are known to govern the behavior of ferrofluids at stronger magnetic fields. The magnetic pattern with the transported paramagnetic object on top is then placed in the center of a goniometer. Both, a sketch and an actual picture of the setup are shown in Fig. 1d and e, respectively. The goniometer holds two large NbB-magnets that generate the external field. The magnets are aligned parallel to each other and create an external magnetic field of magnitude $\mu_0 H_{\mathrm{ext}}$ = 45 mT that penetrates the two-dimensional pattern, the steel sphere, the wax/magnetite spheres, and the ferrofluid droplets. The dipolar interactions between two wax/magnetite spheres or between ferrofluid nanoparticles are weak compared to the interaction with the pattern and the external field.

The gradient of the magnitude of the external field at the position of the transported objects $\nabla H_{\mathrm{ext}} \approx M_{\mathrm{ext}} t_{\mathrm{ext}} {d_{\mathrm{ext}}}^2 / R^4$ is at least two orders of magnitude smaller than that of the magnetic field of the pattern $\nabla H_{\mathrm{p}} \approx (M_{\mathrm{l}} + M_{\mathrm{s}})/a$. Hence, the field created by the external magnets is effectively uniform. The two external magnets can be oriented to produce an arbitrary direction of the external magnetic field with respect to the pattern. A laser pointing along H_{ext} is mounted on the goniometer, see Fig. 1e, to create a stereographic projection of the instantaneous external magnetic field direction on the recording plane.

3 Topologically nontrivial transport loops

The parametric dependence of the potential acting on a paramagnetic object (eqn (2)) was studied in detail in ref. 17. The potential has a hexagonal symmetry and the number of minima per unit cell of the potential can be one or two, depending on the orientation of the uniform external field. The set of possible orientations of the external field forms a sphere that we call the control space $\mathcal{C}$ (see Fig. 2b). Two minima exist in the excess region of $\mathcal{C}$ (see Fig. 2b) in which the orientation of the external field is roughly antiparallel to the magnetization $\mathbf{M}_{\mathrm{l}}$ of the silver magnets in Fig. 2a. Only one minimum of the potential exists for the orientations of the external field roughly parallel to the magnetization of silver magnets (see the green region of the control space in Fig. 2b). The boundary in $\mathcal{C}$ between the excess region and the region of one single minimum is a closed curve in $\mathcal{C}$ that we call the fence $\mathcal{F}$. The fence consists of twelve segments (red and blue in Fig. 2b) meeting in twelve bifurcation points. These bifurcation points ($\mathcal{B}_{+a_i}$, and $\mathcal{B}_{+Q_i}$) are located in the southern hemisphere of $\mathcal{C}$ on longitudes running through the directions $\pm\mathbf{a}_i$ and $\pm\mathbf{Q}_i$ (i = 1, 2, 3) of the primitive unit vectors of the direct and reciprocal lattice, respectively (see Fig. 2a and b). The fence segments are of two types +**Q**-segments (red segments in Fig. 2b) and −**Q**-segments (blue segments in Fig. 2b).

We reorient the external magnets by moving along a closed reorientation loop that starts and ends at the same orientation. (See the black point in Fig. 2b marked as the starting point between $\mathbf{Q}_2$ and the $\mathbf{a}_3$ longitude in the southern unique minimum region.) As a result of the reorientation loop of the external field, the steel sphere, the wax/magnetite spheres, and the ferrofluid droplets move above the magnetic lattice. A motion of the steel sphere is topologically trivial when the sphere responds to a closed reorientation loop with a closed loop on the lattice. Not every closed reorientation loop causes such a trivial response of the steel sphere. There are topologically nontrivial trajectories, where the steel sphere ends at a position differing from the initial position by one unit vector of the magnetic lattice. Nontrivial closed reorientation loops in control space are those loops that have loop segments in both the excess region and the region of the unique minimum.[17,21] Here, the reorientation loop enters the excess region with a longitude ϕ_{entry} between the $\mathbf{Q}_2$ and the $-\mathbf{a}_2$ directions and exits the excess region between the $\mathbf{Q}_2$ and the $\mathbf{a}_3$ longitudes at $\phi_{\mathrm{exit}} = 4.4\pi/6$. The schematic reorientation loops in control space are depicted in Fig. 2b.

3.1 Single steel sphere transport

We have reported in ref. 17, 21 and 22 how the transport of a single paramagnetic particle changes as we move the entry longitude $4.4\pi/6 < \phi_{\mathrm{entry}} < 8.5\pi/6$ of the reorientation closed loop. Here we briefly repeat the findings which are important for this work. The steel sphere adiabatically returns to its initial position (performs a closed loop above the lattice) if the reorientation loop enters and exits the excess region *via* the same fence segment. As an example of such a loop we have drawn the loop a in Fig. 2b for which $\phi_{\mathrm{entry}} = \phi_{\mathrm{exit}} = 4.4\pi/6$. The sphere also returns to the same position when the reorientation loop encloses only the bifurcation point $\mathcal{B}_{a_3}$ or the two bifurcation points $\mathcal{B}_{a_3}$ and $\mathcal{B}_{-Q_1}$ in $\mathcal{C}$ such as in the case of loops b–e ($5\pi/6 < \phi_{\mathrm{entry}} < 7\pi/6$ and $\phi_{\mathrm{exit}} = 4.4\pi/6$) in Fig. 2b. However, as the modulation loop encloses $\mathcal{B}_{a_3}$ the motion is no longer adiabatic. Instead, an irreversible ratchet jump occurs as the modulation loop exits the excess region through the fence.

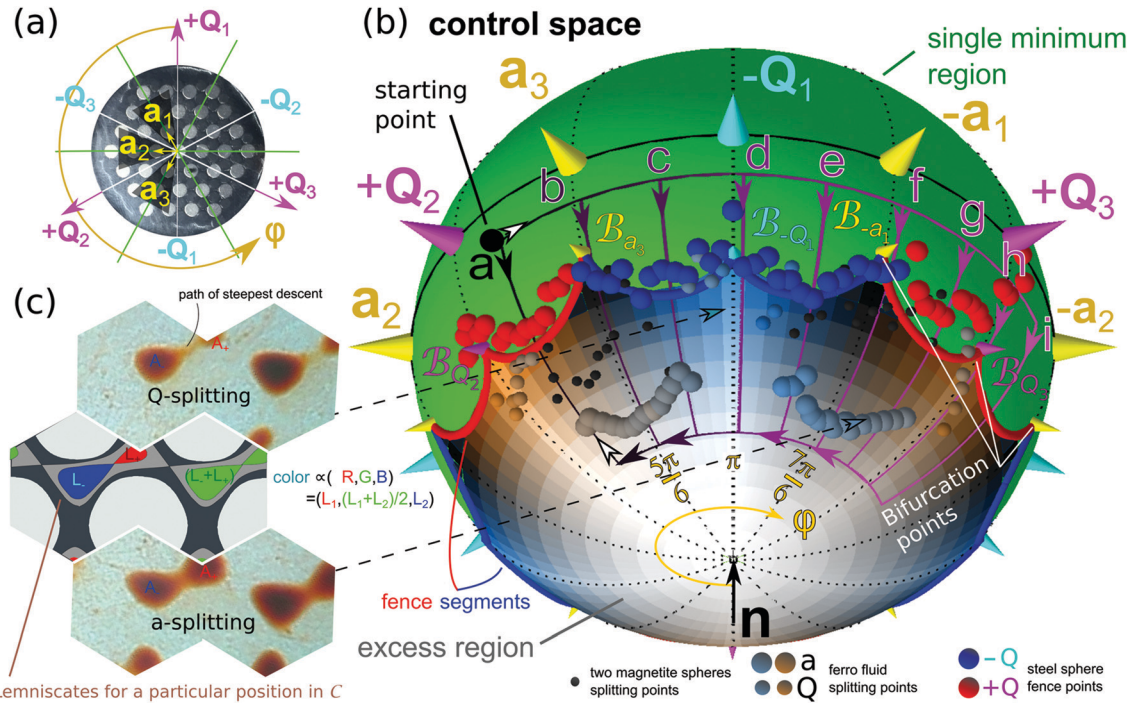

Fig. 2 Orientation of the pattern, the corresponding orientations of the external field in control space and the different events occurring for single steel spheres, wax/magnetite-doublets, and ferrofluid droplets upon the family of modulation loops applied in the experiments. (a) Direction of the primitive unit vectors $\mathbf{a}_1$, $\mathbf{a}_2$, and $\mathbf{a}_3$ of the direct lattice and direction of the primitive unit vectors $\mathbf{Q}_1$, $\mathbf{Q}_2$, and $\mathbf{Q}_3$ of the reciprocal lattice. (b) Control space of the hexagonal lattice. Theoretical fences between the region of one unique minimum (green) and the excess region for paramagnetic objects are shown as red (+**Q** segments) and blue (−**Q** segments) lines. The experimental fence data from the single steel spheres are shown as red and blue spheres. The experiments are performed with modulation loops (a–i) that start at the big black circle (starting point) and enter the excess region in the south of $\mathcal{C}$ along a longitude between the $\mathbf{Q}_2$ and the $-\mathbf{a}_2$ longitudes through either a red or blue fence segment. The loops exit this region and return to the starting point through the red fence along a longitude between $\mathbf{a}_3$ and $\mathbf{Q}_2$. We also used the time reversed loop −i of the loop i. We measure the transport of paramagnetic objects on the pattern as a function of the entry longitude that we continuously vary as a function of the azimuthal angle ϕ_{entry}. The experimentally color coded spheres show the measured splitting location of the ferrofluid droplets and of wax/magnetite doublets, see the legend. The color decodes the different sizes of the split objects according to eqn (3). The same color coding with the droplet areas replaced by the subareas of the theoretical lemniscates is used for the background in the excess region. The unit vector **n** is normal to the pattern. (c) Two unit cells with experimental ferrofluid droplets at a **Q**-splitting line for $\phi_{\text{entry}} \approx \pi$ (top). Two unit cells of the pattern with theoretical lemniscates (equipotential lines through saddle points), computed from the magnetic potential for an external field in the excess region (middle). Two unit cells with experimental ferrofluid droplets at an **a**-splitting line on the loop g for $\phi_{\text{entry}} \approx 7.5\pi/6$ (bottom). The dashed arrows point at the corresponding orientations of the external field in $\mathcal{C}$. A video clip clarifying the details of this figure is provided in the ESI† (adfig2.mp4).

A ratchet occurs if the entry and the exit fence segments are of different types. The motion is always adiabatic if the control loop enters and exits the excess region *via* the same type of fence segments, either +**Q**-segments or −**Q**-segments.[17,21] Here, the motion of the steel sphere returns to adiabatic when enclosing the third bifurcation point $\mathcal{B}_{-a_1}$ (loops f–i $7\pi/6 < \phi_{\text{entry}} < 9\pi/6$ in Fig. 2b) with a total displacement of the sphere by one unit vector $-\mathbf{a}_2$. Since this reorientation loop is adiabatic, the time reversed loop (*e.g.* the inverse loop −h with $4\pi/6 < \phi_{\text{entry}} < 5\pi/6$ and $7\pi/6 < \phi_{\text{exit}} < 8\pi/6$) transports into the opposite, *i.e.* the $\mathbf{a}_2$ direction compared to the direct loop. We have measured the position of the fence in control space *via* the ratchet jumps of the steel sphere. The blue and red spheres in Fig. 2b are the experimental data of these measurements.

3.2 Ferrofluid droplet transport

In Section 3.1, we described the limiting case of one particle being transported. Here, we describe the opposite limit, namely the transport of a macroscopic ensemble of particles. The particle numbers in between describe the transition from topological towards geometrical and they are discussed in Sections 3.3 and 3.4. To mimic the transport in a system with hundreds of tiny particles per unit cell, we consider the motion of ferrofluid droplets. Hence, the transported object can no longer be considered a point particle. To understand the motion, we need to consider the equipotential lines around the minima of the total magnetic potential that drives the motion. In Fig. 3 we collect images that show the motion of a ferrofluid droplet along some of the control modulation loops displayed in Fig. 2. The loops enclose from zero up to four bifurcation points. At the starting point, the steel sphere and the ferrofluid droplets reside above the central magnet of the unit cell. The sphere/droplet moves away from this location as the external magnetic field enters into the excess region of $\mathcal{C}$. Nothing special occurs when the external field crosses the fence, and nothing particular happens to the single steel sphere as the

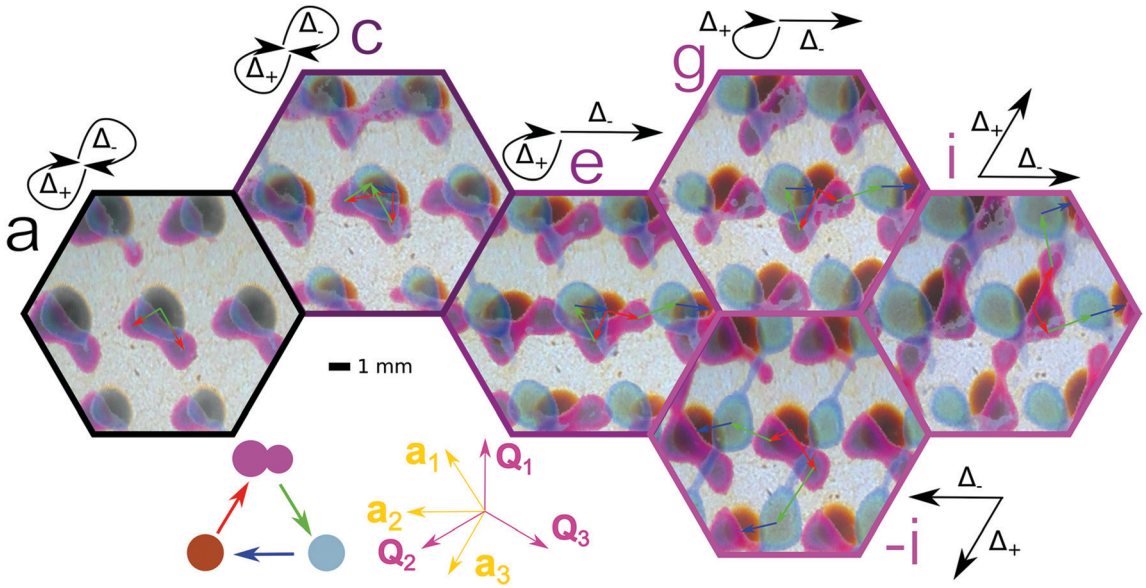

Fig. 3 Dynamics of the ferrofluid droplets subject to the modulation loops a-i, and −i of Fig. 2. In each image we overlay an image of the droplet before the entry into the excess region (brown), at the splitting line (purple) and after recombination at the end of the loop (turquoise). The different images correspond to different loops depicted in Fig. 2b with loop a $\phi_{entry} = \phi_{exit} = 4.4\pi/6$, loop c $\phi_{entry} = 5.5\pi/6$, $\phi_{exit} = 4.4\pi/6$, loop e $\phi_{entry} = 6.5\pi/6$, $\phi_{exit} = 4.4\pi/6$, loop g $\phi_{entry} = 7.5\pi/6$, $\phi_{exit} = 4.4\pi/6$ loop i $\phi_{entry} = 8.5\pi/6$, $\phi_{exit} = 4.4\pi/6$ and the inverse loop −i $\phi_{entry} = 4.4\pi/6$, $\phi_{exit} = 8.5\pi/6$. For loops a and c, two trivial modes coexist. In loops e and g, a transport mode into the $-\mathbf{a}_2$ direction coexists with a trivial mode. In loop i, a transport mode in the $-\mathbf{a}_2$ direction coexists with a transport mode into the $-\mathbf{a}_3$ direction. The control loop of −i is the inverse of loop i with two transport modes along $\mathbf{a}_2$ and $\mathbf{a}_3$. The red arrows show the transport directions during the splitting of the brown droplet towards the purple droplets. The green arrows show the motion of the two purple droplets as they rejoin into the turquoise droplet. The blue arrow shows the adiabatic motion upon closing the loop in control space by returning to the starting point. The displacement after one control loop is the coexistence of the two displacements $\mathbf{\Lambda}_+$ and $\mathbf{\Lambda}_-$ of the two split droplets. The black arrows are sketches of the motion of the droplets. The scale bar is 1 mm. A video clip showing the motion of the droplets is provided in the ESI† (adfig3.mp4).

field moves deeper into the excess region. The ferrofluid droplet, however, deforms into a dogbone-like shape and eventually splits into two smaller droplets when the modulation loop crosses a droplet splitting line in $\mathcal{C}$. Some of the shapes of such droplets are shown in Fig. 2c. Their shape and size agree very well with the shape and size of the lemniscates, which are simply the equipotential lines of the colloidal potential passing through the saddle point between both minima (see Fig. 2c). The two separated ferrofluid droplets reside in a region above the two different minima, where the potential is in the excess region of $\mathcal{C}$. The droplets are in general transported into different directions. When the modulation loop is closed (returns to the starting point), the two split ferrofluid droplets must return to either the original position above the same central silver magnet or to an equivalent position in a different unit cell. The transport over one period is therefore the coexistence of two different types of transport directions. The total transport is the sum of the two coexisting displacements, weighted with the two areas of the droplets when they split.

The splitting of a ferrofluid droplet occurs either in an adiabatic way (**a**-splitting) or irreversibly (**Q**-splitting). Both types of splitting are schematically represented in Fig. 4. The ferrofluid droplet covers a certain area A of action space when the external field enters the excess region of $\mathcal{C}$. A "minor" excess minimum and an excess saddle point are created in the magnetic potential upon the entry of the external field into the excess region.[17] The equi-potential line passing through the excess saddle point is a lemniscate that first winds around the preexisting "major" minimum, then passes through the saddle point, and next winds around the minor excess minimum. Hence, the lemniscate defines a closed curve of area $L = L_+ + L_-$ where each of the two sub areas, L_+ and L_-, surrounds a minimum of the potential. At the fence in $\mathcal{C}$, the sub lemniscate area of the minor minimum, $L_+ = 0$ ($L_- = 0$) for a $-\mathbf{Q}$-fence segment ($+\mathbf{Q}$-fence segment) vanishes. At the fence $L_+ = 0$ or $L_- = 0$ and the area occupied by the ferrofluid droplet can be either larger $A > L_+ + L_-$ or smaller $A < L_-$ ($A < L_+$) than that of the preexisting major minimum.

In the case $A > L_+ + L_-$ (**a**-splitting), which occurs if the loop enters the excess region of $\mathcal{C}$ close to a $\mathcal{B}_a$ bifurcation point, the ferrofluid droplet assumes the shape of an equipotential line containing both minima (see Fig. 2c bottom and Fig. 4a). When the loop enters deeper into the excess region of $\mathcal{C}$, the area of the lemniscate grows (Fig. 4(a1) and (a2)). At the point where the area of the lemniscate is the same as the area of the droplet, $L = L^a = A$, both lemniscate subareas L^a_+ and L^a_- are fully filled with a ferrofluid (Fig. 4(a3)). When the area of the lemniscate grows beyond that of the droplet, $L > A$, then the droplet splits into two droplets of areas $A_+ = L^a_+$ and $A_- = L^a_-$ (Fig. 4(a4)). The areas of both droplets do not change until the droplets coalesce again, *i.e.* no further splitting occurs. The splitting is reversible if the control loop is reversed and crosses the splitting line $L^a = A$ at exactly the same point.

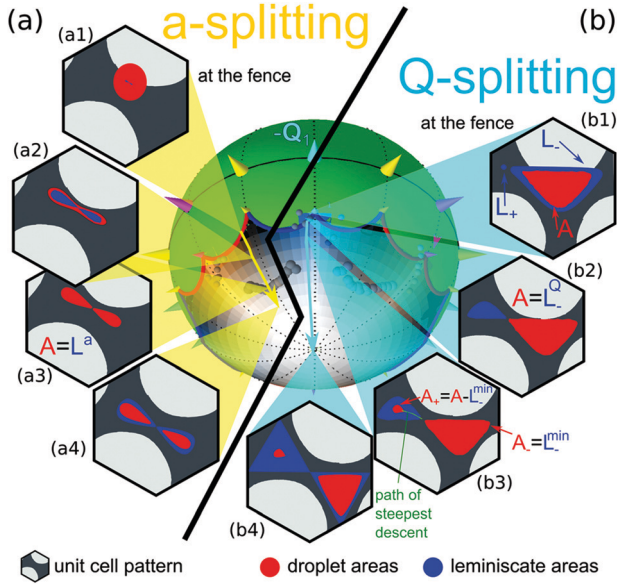

Fig. 4 Schematics of the **a**-splitting (a) and the **Q**-splitting (b) of a ferrofluid droplet. In each case a unit cell (hexagon) with the droplets (red) and the lemniscates (blue) is represented for four different orientations of the external field along a control loop that enters the excess regions of $\mathcal{C}$ near a $\mathcal{B}_a$-bifurcation point (a1)–(a4) and a $\mathcal{B}_{-Q}$-bifurcation point (b1)–(b4). The loop segments of both loops in control space are indicated in the control space in the center of the image. The positions of the large (small) magnets in the unit cell are shown in light (dark) gray.

In Fig. 2b we have color coded the splitting ferrofluid droplets with a normalized RGB-color given by the triplet

$$(\mathrm{R},\mathrm{G},\mathrm{B}) = \frac{8}{A_{\mathrm{UC}}}(A_+, (A_+ + A_-)/2, A_-), \qquad (3)$$

where A_{UC} is the area of the unit cell, and the factor eight accounts for the fact that the maximum subarea of a lemniscate is one eighth of the area of the unit cell (see Fig. 4(b4)). We have also color coded the excess region of $\mathcal{C}$ in Fig. 2b with the same criterion but replacing the subareas $A_\pm$ with the subareas of the lemniscates $L_\pm$. Hence, the color of the experimental data points at the splitting lines in Fig. 2b matches the color of the control space only if $A_\pm = L_\pm$, *i.e.*, if the subareas of the theoretical lemniscates and those of the droplets are equal. In Fig. 2b, the color of the experimental **a**-splitting points is darker than the background, indicating that the experimental droplets split later than predicted by the theory. This is presumably because adhesive forces of the droplet prevent early splitting. The color discrepancy of the data below the $\mathcal{B}_{-a_1}$ bifurcation points is likely due to scattering in the magnetization of the NbB magnets forming the pattern. The finite size of the pattern and the elevation of the particles above the pattern also have an effect on the experimental measurements.

In the case $A < L_-$ ($-$**Q**-splitting), which occurs if the control loop enters the excess region close to a $\mathcal{B}_{-Q}$ bifurcation point, the ferrofluid droplet assumes the shape of an equi-potential line surrounding only the preexisting major minimum but not the excess minor minimum. We show in Fig. 2c top the picture of a droplet just after a $-$**Q**-splitting (see also Fig. 4b). The largest areas of L_- occur if the external field points at the south pole and at the $\mathcal{B}_{-Q}$ bifurcation points of $\mathcal{C}$. Hence, a locally minimal area $L_-^{\min}$ occurs for external fields pointing along a longitude that connects the south pole and one of the $\mathcal{B}_{-Q}$ bifurcation points. The subarea L_- of the preexisting minimum of the lemniscate shrinks as the control loop moves from the fence towards the south pole (Fig. 4(b1)). At some point, the subarea of the lemniscate L_- equals that of the droplet $L_-^Q = A$ (provided that $L_-^{\min} < A < L_-$), Fig. 4(b2). There, the fluid completely fills the subarea L_-^Q while the other subarea L_+ is completely empty. When the major area of the lemniscate shrinks below the droplet area, *i.e.* $L_- < A$, then the droplets split into two droplets of areas $A_- = L_-$ and $A_+ = A - L_-$ (Fig. 4(b3)). The fluid in L_- is expelled from the droplet through the saddle point and flows down the path of the steepest descend into the basin of the minor excess minimum. The areas of the droplet change until the decrease of L_- stops, Fig. 4(b4). The splitting process is irreversible and both droplets cannot be rejoined in a reversible way since the fluid in the excess minimum cannot flow up the path of the steepest descent back into the preexisting minimum.

We have placed $\pm$**Q**-splitting experimental points at the location where the splitting starts. The points are colored according to eqn (3) with $A_\pm$ being the subareas when the interchange of fluid between A_+ and A_- stops. The agreement with the theoretical prediction given by the areas of the lemniscate (colored background) is excellent.

The splitting lines $L^a = A$, $L_-^Q = A$ and $L_+^Q = A$ are the segments of a closed curve that are joined at the fence of $\mathcal{C}$. For $A > L_-^{\min}$, any closed curve of a modulation loop in $\mathcal{C}$ that penetrates the excess region deep enough must also pass the splitting curve. A nontrivial modulation therefore causes nontrivial transport that is the coexistence of two topological displacements weighted with the two split areas of the droplet. The splitting areas A_- and A_+ continuously change along the splitting lines. A video clip (adfig3.mp4) showing more details of the ferrofluid transport is provided in the ESI.†

3.3 Doublet transport

We have experimentally studied the transport of two particles per unit cell. The area A enclosed by the two wax/magnetite spheres is smaller than the local minimum area, *i.e.* $A < L_-^{\min}$. Hence, in contrast to the ferrofluid droplet, the Q-splitting cannot occur for these doublets. Both the ferrofluid droplet and the doublet exhibit **a**-splitting. A measurement of the **a**-splitting line $L^a = A$ is shown for the wax/magnetite doublets in Fig. 2b. The doublets are transported together within the major minimum if the control loop enters the excess region in the vicinity of the $\mathcal{B}_{\pm Q}$ bifurcation point. If the loop enters the excess region in the vicinity of the $\mathcal{B}_a$ bifurcation point, then **a**-splitting occurs and both spheres are separated. One sphere is transported within the major minimum and the other one within the minor minimum. Two transport directions coexist.

Hence, depending on ϕ_{entry} there are two different transport modes for the doublets: (i) no splitting and (ii) **a**-splitting. The

transition from one transport mode towards the other transport mode occurs at the doublet bifurcation points $\mathcal{B}_{\text{doublet}}$ that are the intersections of the fence with the **a**-splitting line $L^a = A$ for doublets. Since the spheres have the same size, the areas of the **a**-splitting transport are equal $A_- = A_+ = A/2$. Hence, the experimental data points for doublet **a**-splitting all have the same color, see eqn (3) and Fig. 2b. The color is darker than the theoretical background color of the lemniscates. Hence, splitting occurs later in the experiment than predicted by the theory, presumably due to the dipolar attraction between the two spheres as well as due to friction with the bottom surface. Like the transport of a single sphere, the transport of doublets is discrete and therefore topological.

Net displacement. We next analyze the net displacement after the completion of one entire control loop for all three types of objects: single spheres, doublets, and ferrofluid droplets. For all objects, we define the vector of the net displacement $\mathbf{\Delta}$ as the area averaged sum of the two possible displacements. That is

$$\mathbf{\Delta} = \frac{\mathbf{\Delta}_+ A_+ + \mathbf{\Delta}_- A_-}{A_+ + A_-}, \tag{4}$$

where $\mathbf{\Delta}_\pm$ are the net displacement vectors of the two minima in one control loop. Hence, $\mathbf{\Delta}_\pm$ are always lattice vectors and $\mathbf{\Delta}$ moves along a straight line between the two lattice vectors.

In Fig. 5a, we plot the net displacement of all magnetic objects as a function of ϕ_{entry} for a family of loops with $\phi_{\text{exit}} = 4.4\pi/6$ (loops similar to those in Fig. 2b). A video of the motion is presented in the ESI† (adfig5.mp4). The net displacement is zero when the loop encloses no bifurcation point. The displacement moves along the straight lines connecting the sequence of lattice vectors $\mathbf{0}, -\mathbf{a}_2, -\mathbf{a}_3, \mathbf{a}_1$, and $\mathbf{0}$ (see the gray arrows in the center of Fig. 5a). The areas A_+ and A_- are continuous functions of ϕ_{entry} for the ferrofluid droplet. In contrast, the transported

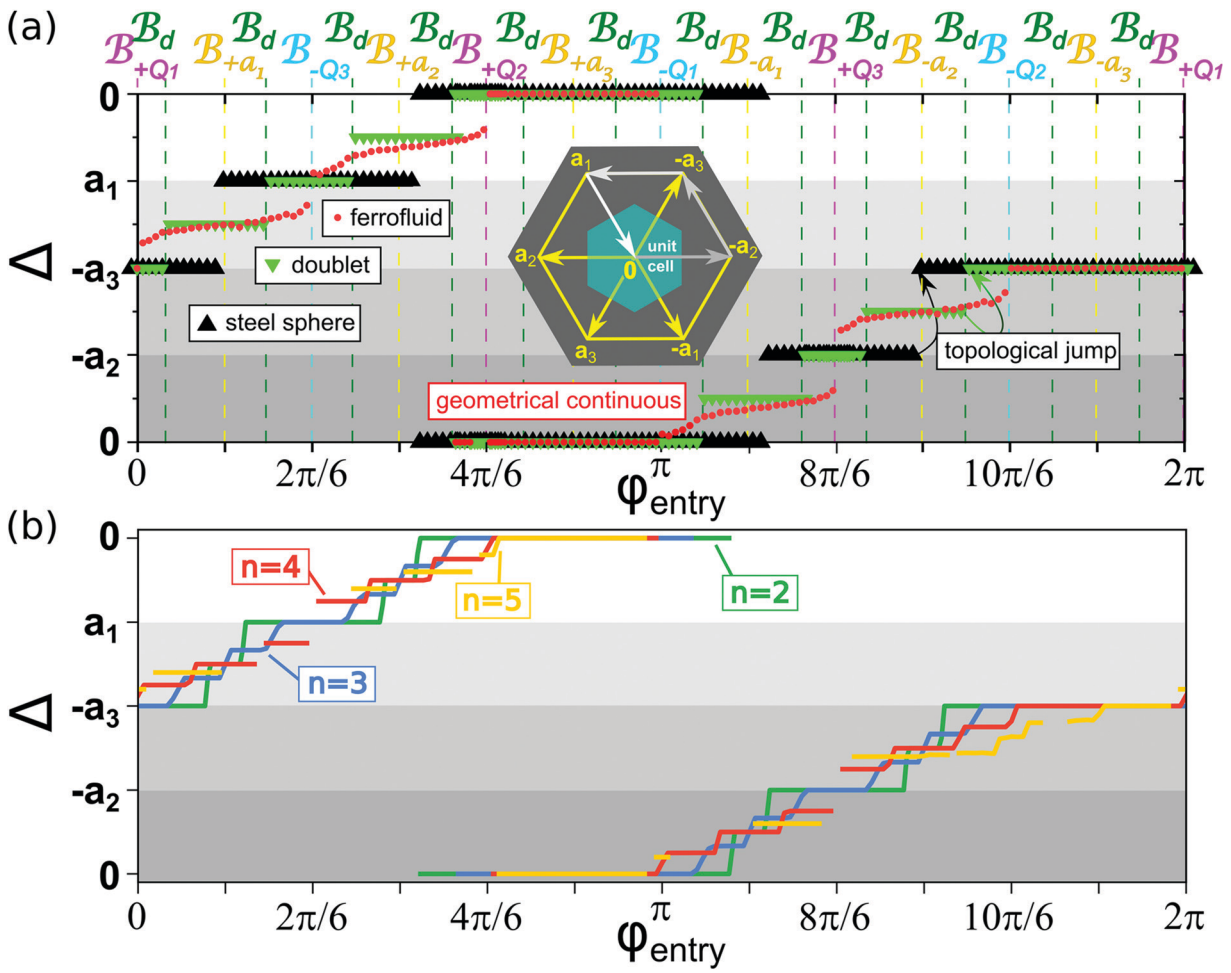

Fig. 5 Experimental and simulated displacements for the set of modulation loops characterized by ϕ_{entry}. (a) Experimental measurements of the net displacement $\mathbf{\Delta}$ of the steel sphere, the wax/magnetite doublet, and the ferrofluid droplets as a function of ϕ_{entry} for a family of loops with $\phi_{\text{exit}} = 4.4\pi/6$. The displacement changes correspond to the four gray arrows shown in the center of the image. The four gray shaded regions correspond to the arrows of the same color in the inset. The displacement is a discrete function of ϕ_{entry} for the steel sphere and the wax/magnetite spheres but a continuous function for the ferrofluid droplets. The jumps in the displacement occur when the loop crosses the bifurcation points in control space (the position of the bifurcation points is indicated with vertical dashed lines). A video of the motion of a steel sphere, a wax magnetite doublet, and ferrofluid droplets subjected to two different control loops is shown in the ESI† adfig5.mp4. (b) Net displacement of a collection of n = 2, 3, 4, and 5 particles, as indicated, for the same family of control loops as in panel (a) according to computer simulations.

areas $A_{\pm}$ for one steel sphere (a wax/magnetite doublet) can only be integer multiples n = 0,1 (n = 0,1,2) of the area of one sphere. Contrary to the ferrofluid transport, the sphere and doublet net displacement change discretely with ϕ_{entry}. The number of discrete steps for the doublets is twice that of a single steel sphere. Hence, the transport of one or two spheres is topological while the transport of the ferrofluid is geometrical.

3.4 Multiparticle transport

What is the minimum number of particles required for having geometrical transport? To address this fundamental question, we have simulated the transport of multiple spheres using overdamped Langevin dynamics (note that inertial effects are negligible). Each unit cell is filled with exactly n particles. Each particle is subject to the magnetic potential

$$U(\mathbf{x}_{\mathcal{A}}, \mathbf{H}_{\mathrm{ext}}(t)) \propto -\mathbf{H}_{\mathrm{ext}}(t) \cdot \mathbf{H}_{\mathrm{p}}(\mathbf{x}_{\mathcal{A}}), \tag{5}$$

where $\mathbf{H}_{\mathrm{ext}}(t)$ is the external field at time t and $\mathbf{H}_{\mathrm{p}}(\mathbf{x}_{\mathcal{A}})$ is the magnetic field, created by the pattern at the position of the particle $\mathbf{x}_{\mathcal{A}}$ in action space $\mathcal{A}$, see ref. 22 and 23.

The particles interact *via* the purely repulsive Weeks–Chandler–Andersen potential

$$\phi(r) = \begin{cases} 4\varepsilon\left(\left(\frac{\sigma}{r}\right)^{12} - \left(\frac{\sigma}{r}\right)^{6} + \frac{1}{4}\right) & r \le 2^{1/6}\sigma \\ 0 & r > 2^{1/6}\sigma \end{cases}, \tag{6}$$

where r is the distance between the particles, ε fixes our unit and energy, and σ is the effective particle length that we fix to σ/a = 0.2 which is the same as in the experiments (transport of single spheres). We integrate the equations of motion with a time step $\mathrm{d}t/T = 10^{-5}$, with T being the period of a modulation loop. As the transport is topological the detailed features of the simulated particles are of minor importance and the behavior will not change using somewhat different parameters for the simulations. Fig. 5b shows the net displacement of n = 2, 3, 4, 5 spheres. The number of plateaus in the displacement of n particles per unit cell is n times the number of plateaus of a single sphere. This is true provided that each unit cell is filled with precisely n particles since the results depend on the initial distribution of particles among the different unit cells. Our simulation results suggest therefore that if precisely the same number of equally sized ferrofluid particles could be deposited in each droplet, one would still observe topological transport, albeit with very fine splitting. However, if there is dispersion in the size of particles, the occupation of the unit cells, the number of plateaus and splittings might be significantly increased because the number of different geometrically distinguishable ways to split the droplets into subdroplets is increased. For broad dispersions of sizes we would expect that the transport is topological with a step size that scales with an other power than the inverse of the occupation of the site. Here, we have investigated only the case of monodisperse particles.

Note that the experimental ϕ_{entry} and the ϕ_{entry} in the simulations of the doublet bifurcation points (at which the net displacement jumps) differ (Fig. 5a and b). In the experiment, the spheres do not only interact *via* excluded volume interactions, but are also subject to long range dipolar interactions. We tried to minimize the effect of dipolar interactions by using the wax/magnetite composite spheres. We have understood the transport properties under simple conditions, however an in depth understanding must also include studies of how the transport changes with polydisperse particle sizes, varying the occupation of unit cells, and with stronger dipolar interactions.

4 Conclusions

We have studied experimentally and with computer simulations the transport of paramagnetic particles on top of a magnetic lattice, driven by a uniform and time-dependent external magnetic field. The external field performs periodic closed loops. We have shown that increasing the number of particles within the unit cell of the lattice changes the transport from topological towards geometrical.

The transport as a function of a parameter that continuously characterizes a family of control loops is discrete for low particle densities and continuous for a macroscopic number of particles per unit cell (ferrofluid droplet). More possibilities to split or disjoin soft matter assemblies increase the number of bifurcation points in control space with more transport modes in action space that are separated by finer steps. It is the number of possibilities that eventually changes the transport from topological to geometrical.

A ferrofluid is a colloidal suspension of nanoparticles. Rendering the transport of this soft matter system as robust as the solid particle transport, the magnetic pattern must be downscaled to the nanometer range. In such downscaling studies, we have already shown the topological nature of the transport of a colloidal dispersion of micron-sized magnetic colloids.[17,22]

Conflicts of interest

There are no conflicts to declare.

Appendix

Here we provide some details of the experimental setup. The magnetic hexagonal lattice (Fig. 1a) consists of large (l) and small (s) cylindrical magnets of height h = 2 mm, diameters d_{l} = 3 mm and d_{s} = 2 mm, and remanences $\mu_0 M_{\mathrm{l}}$ = 1.19 T and $\mu_0 M_{\mathrm{s}}$ = 1.35 T, with μ_0 being the permeability of free space. The resulting lattice with two primitive lattice vectors of length a = 4.33 mm is mechanically metastable in zero external magnetic field. Therefore, we need to fix the metastable arrangement with an epoxy resin placed in the voids and in the two dimensional surroundings of the pattern. The pattern is then stable also in the presence of an external field. The pattern is put on a support and covered with a transparent PMMA spacer of thickness z = 1–1.5 mm (Fig. 1c). It may be sprayed with PTFE to suppress wetting with the ferrofluid

droplets. Additionally, a white illuminated foil can be placed underneath the PMMA.

We either place one steel sphere of diameter $2r$ = 1 mm or two spheres of diameter $2r$ = 0.5 mm consisting of a 10 : 1 weight percent mixture of wax and magnetite on top of the spacer. Alternatively, we place two fluids, a nonmagnetic fluid (Galden) and an aqueous ferrofluid immiscible with the Galden at a volume ratio Galden/ferrofluid of 152 : 1, on top of the PTFE and close to the compartment with a transparent lid.

The goniometer is set up at an angle of 45 degrees to ensure that the relevant motion is not affected by the restrictions of motion of the goniometer caused by the support. The two large NbB-magnets that generate the external field have a diameter d_{ext} = 60 mm, a thickness t_{ext} = 10 mm, and a remanence of $\mu_0 M_{ext}$ = 1.28 T and they are separated by a distance $2R$ = 120 mm.

Acknowledgements

Scientific discussion with Michel Lönne is highly appreciated.

References

1 S.-Q. Shen, *Topological insulators: Dirac equation in condensed matters*, Springer Science, and Business Media, 2013.
2 J. Anandan, J. Christian and K. Wanelik, Resource Letter GPP-1: Geometric Phases in Physics, *Am. J. Phys.*, 1997, **65**, 180–185.
3 M. V. Berry, Quantum phase factors accompanying adiabatic changes, *Proc. R. Soc. London, Ser. A*, 1984, **A392**, 45–57.
4 J. H. Hannay, Angle variable holonomy in adiabatic excursion of an integrable Hamiltonian, *J. Phys.*, 1985, **A18**, 221–230.
5 A. Shapere and F. Wilczek, Geometry of self-propulsion at low Reynolds number, *J. Fluid Mech.*, 1989, **198**, 557–585.
6 A. Shapere and F. Wilczek, Efficiency of self-propulsion at low Reynolds number, *J. Fluid Mech.*, 1989, **198**, 587–599.
7 M. Z. Hasan and C. L. Kane, Colloquium: Topological insulators, *Rev. Mod. Phys.*, 2010, **82**, 3045–3067.
8 D. Harland and N. S. Manton, Rolling Skyrmions and the nuclear spin-orbit force, *Nucl. Phys. B*, 2018, **935**, 210–241.
9 K. v. Klitzing, G. Dorda and M. Pepper, New method for high-accuracy determination of the fine-structure constant based on quantized Hall resistance, *Phys. Rev. Lett.*, 1980, **45**, 494–497.
10 M. C. Rechtsman, J. M. Zeuner, Y. Plotnik, Y. Lumer, D. Podolsky, F. Dreisow, S. Nolte, M. Segev and A. Szameit, Photonic Floquet topological insulators, *Nature*, 2013, **496**, 196–200.
11 M. Xiao, G. Ma, Z. Yang, P. Sheng, Z. Q. Zhang and C. T. Chan, Geometric phase and band inversion in periodic acoustic systems, *Nat. Phys.*, 2015, **11**, 240–244.
12 J. Paulose, B. G. Chen and V. Vitelli, Topological modes bound to dislocations in mechanical metamaterials, *Nat. Phys.*, 2015, **11**, 153–156.
13 C. L. Kane and T. C. Lubensky, Topological boundary modes in isostatic lattices, *Nat. Phys.*, 2014, **10**, 39–45.
14 L. M. Nash, D. Kleckner, A. Read, V. Vitelli, A. M. Turner and W. T. M. Irvine, Topological mechanics of gyroscopic metamaterials, *Proc. Natl. Acad. Sci. U. S. A.*, 2015, **112**, 14495–14500.
15 S. D. Huber, Topological mechanics, *Nat. Phys.*, 2016, **12**, 621–623.
16 A. Murugan and S. Vaikuntanathan, Topologically protected modes in non-equilibrium stochastic systems, *Nat. Commun.*, 2017, **8**, 13881.
17 J. Loehr, M. Loenne, A. Ernst, D. de las Heras and T. M. Fischer, Topological protection of multiparticle dissipative transport, *Nat. Commun.*, 2016, **7**, 11745.
18 Y. Xiong, Why does bulk boundary correspondence fail in some non-hermitian topological models, *J. Phys. Commun.*, 2018, **2**, 035043.
19 S. Yao and Z. Wang, Edge States and Topological Invariants of Non-Hermitian Systems, *Phys. Rev. Lett.*, 2018, **121**, 086803.
20 F. K. Kunst, E. Edvardsson, J. C. Budich and E. J. Bergholtz, Biorthogonal bulk-boundary correspondence in non-Hermitian systems, *Phys. Rev. Lett.*, 2018, **121**, 026808.
21 A. M. E. B. Rossi, J. Bugase and T. M. Fischer, Macroscopic Floquet topological crystalline steel and superconductor pump, *Europhys. Lett.*, 2017, **119**, 40001.
22 J. Loehr, D. de las Heras, M. Loenne, J. Bugase, A. Jarosz, M. Urbaniak, F. Stobiecki, A. Tomita, R. Huhnstock, I. Koch, A. Ehresmann, D. Holzinger and T. M. Fischer, Lattice symmetries and the topologically protected transport of colloidal particles, *Soft Matter*, 2017, **13**, 5044–5075.
23 D. de las Heras, J. Loehr, M. Loenne and T. M. Fischer, Topologically protected colloidal transport above a square magnetic lattice, *New J. Phys.*, 2016, **18**, 105009.
24 D. P. Jackson, R. E. Goldstein and A. O. Cebers, Hydrodynamics of fingering instabilities in dipolar fluids, *Phys. Rev. E: Stat. Phys., Plasmas, Fluids, Relat. Interdiscip. Top.*, 1994, **50**, 298.
25 N. Wilke, J. Bugase, L.-M. Treffenstädt and T. M. Fischer, Wrinkled labyrinths in critical demixing ferrofluid, *Soft Matter*, 2017, **13**, 7307–7311.